

## Research Article

# Study on the Relationship between Mechanical Properties and Mesostructure of Microbial Cemented Sand Bodies

Yue Yan , Yang Tang , Guobin Xu , Jijian Lian , and Dengfeng Fu

State Key Laboratory of Hydraulic Engineering Simulation and Safety, Tianjin University, Tianjin 300072, China

Correspondence should be addressed to Yue Yan; [yueyan\\_geo@126.com](mailto:yueyan_geo@126.com)

Received 28 November 2018; Revised 26 January 2019; Accepted 13 February 2019; Published 4 March 2019

Academic Editor: Charles C. Sorrell

Copyright © 2019 Yue Yan et al. This is an open access article distributed under the Creative Commons Attribution License, which permits unrestricted use, distribution, and reproduction in any medium, provided the original work is properly cited.

Microbial-induced calcite precipitation (MICP) is a novel ground improvement method to effectively increase the strength of sandy soil. However, the relationship between the compressive strength of cemented sand and mesostructure of the cemented structure has not been addressed adequately. In this paper, a suite of microbial cementing experiments were conducted, considering multiple parameters controllable in testing. Twenty-two cementing columns were examined by uniaxial compressive strength (UCS) tests to explore the response of variations in compressive strength. The correlation of compressive strength with mesostructure of cemented samples was investigated using the X-ray computed tomography (XCT) method. Three main influential factors—the uniform spatial distribution, increasing contents, and increasing size of the crystals—were found to contribute positively to the strength behavior. Under relatively uniform spatial distribution, increasing the contents of crystals facilitated the initial construction of “spatial network” structure, and further stacks of calcium carbonate crystals promote the complete construction of the “spatial network” structure, and thus helped to increase compressive strength. The spatial distribution curves of crystals are in good agreement with the destructive characteristic curves of structures.

## 1. Introduction

Microbial mineralization is a ubiquitous phenomenon in which some microorganisms can use their metabolic activities in nature to produce a variety of mineral crystals. Calcium carbonate is a widely distributed carbonate with relatively stable properties, robust strength and durability, which continues to play a significant role in today’s microbial mineralization research.

At present, the experimental research on microbial-induced calcium carbonate deposition technology based on *Sporosarcina pasteurii* has mainly focused on the mechanical properties of sand soil by microorganisms [1–7]; that is, the mechanical properties of the cemented structure are explored through macroscopic experiments. For the evolution process of mechanical properties of the cemented structure, some scholars explored the influence of environmental factors and mesostructure on structural mechanical behavior, respectively. For example, Cheng et al. [8] studied the influence of key environmental factors on urea

hydrolysis and showed that effective crystal deposition can be obtained under low urease activity, and the produced large clusters could improve the structural strength by filling the voids between the soil particles. Dhama et al. [9] analyzed the microscopic type of crystals in crystal mineralization and showed that the mechanical properties of the material can be improved by controlling the chemical reaction process. These research results are conducive in improving the mechanical properties.

However, for the MICP technology, it has been found that, when bacteria and cementing solution are injected into loose sand body, the length of static time, the flow rate of bacteria, and cementing solution will affect the mechanical properties of the structure [10]; fully comprehensive consideration of multiple influencing factors is of importance [11]. These environmental factors will cause the nature of the mesostructure to be specific. This particularity and its impact on the mechanical properties has not been comprehensively considered in other previous literatures. They are particularly important for the application of MICP techniques in

engineering and for improving structural mechanical properties.

Considering the above highlighted research results, the remainder of the following sections has been organized as follows: First, the orthogonal experiment was designed, considering various experimental controllable factors, including the concentration of bacterial solution, the concentration of cementing fluid, the flow rate of bacterial solution, the flow rate of cementing fluid, the static time of bacterial solution, and the static time of cementing fluid. Second, the physical experimental process of MCS has been introduced briefly. The results obtained using the uniaxial compressive strength (UCS) test were analyzed to investigate the failure mode and stress-strain characteristics of the solidified sand samples under the comprehensive effect of multiple influencing factors. Finally, the correlation mechanism between the mesostructure and mechanical properties of microbial cemented sand bodies was studied, which includes the following: (1) the influence of crystal spatial distribution on structural mechanical strength is investigated; (2) the relationship between spatial distribution of crystals and structural failure modes is established, and simplified models for different spatial distribution of crystals are proposed; (3) the influence of the size of crystal on structural strength is analyzed.

## 2. Experimental Setup

The experimental design, experimental MICP treatment process, uniaxial compressive strength, and textural analysis tests of the MCS material are summarized below.

**2.1. Experimental Design.** The multifactor experimental design method mainly includes the following: orthogonal test design, uniform test design, tuning test design, and regression orthogonal test design. Combined with the characteristics of this cementation test and the actual situation of the laboratory, the orthogonal test [12] was used to study the effect of the coupling of various influencing factors on the mechanical properties of microbial cemented sand bodies.

This paper investigated the effects of six parameters on cementation (Table 1). Designed using L25 ( $5^6$ ) orthogonal table, 25 sets of control variables were combined. The specific orthogonal design test combination working conditions are shown in Table 2.

**2.2. Sample Preparation.** The basic physical properties of standard sand used in this study are shown in Table 3 [13]. The paper briefly introduces the sample preparation method, and the detailed method has been described by Xu et al. [14].

A visible light spectrophotometer (WFJ2000, UNICO) was used to detect the number of microorganisms. The wavelength was 600 nm, and the measured value was  $OD_{600}$ . A cementation solution of urea- $CaCl_2$  was used where the urea was the nitrogen and energy source of microbial growth and  $CaCl_2$  was the calcium source in the process of MICP.

Tests are carried out according to the test conditions designed (Table 2).

Five additions of cementing solutions and one of bacterial liquids were considered one cycle for the entire cementation process, and two cycles were performed for the test sample. The test model size was  $50 \times 100$  mm. The test device is shown in Figure 1.

**2.3. Uniaxial Compressive Strength (UCS) Test.** The UCS testing of the MCS material was conducted using a microcomputer-controlled electrohydraulic servo loading testing machine (TAW-2000) (Figure 2). The maximum loading capacity of the TAW-2000 was 2000 kN. The uniaxial compressive strength test was set to be displacement controlled at a loading rate of 0.05 mm/min until failure occurred. In order to ensure the accuracy of the experimental test, it is necessary to polish both ends of the test sample so as to ensure a flat end face.

**2.4. Textural Analysis Test.** A micro-XCT instrument (diondo d5), a voltage of 180 KV, and tube current of 0.18 mA were used, and the exposure time of the detector was 1000 ms in this study. The experimental process is shown in Figure 3 [13].

## 3. Results and Analysis

**3.1. Analysis of Mechanical Properties of Microbial Cemented Sand Body.** In this section, the mechanical properties of microbial cemented sand body structure were analyzed from the failure mode and stress-strain mechanical behavior of cemented sand body.

**3.1.1. Microbial Cemented Sand Body Structure Uniaxial Compression Failure Mode.** The uniaxial compression failure of the cemented sand column under different control variables is shown in Figure 4. For the samples #1, 3#, and 5#, the compression test was not performed due to lower strength (under test conditions) and only the compression test under the remaining 22 sets of conditions was performed. By observing the damage pictures under various working conditions in the figure, it was found that the damage morphology of the samples was different, the crack shapes were different, and the sample after loading was sensitive to disturbance, revealing a certain fragmentation characteristic.

Under uniaxial compression conditions, the failure modes of sand columns were divided into tensile failure, shear failure, and tensile-shear composite failure. For tensile failure, the damage was mainly from the top to the bottom, and the expansion path was approximately a straight line (8# and 25#). For shear failure, the failure mode mainly occurred along the top of the sand column. The local block was detached and had obvious shear-slip surface features (4#, 9#, and 18#). For the composite failure of the tensile-shear, the damage had observable failure surface and shear-slip

TABLE 1: Orthogonal factor level.

Factor	Factor level					Number
Bacterial concentration ( $M_b$ )	0.25	0.5	1.0	1.5	2.0	5
Bacterial fluid flow ( $Q_b$ )	1 ml/min	3 ml/min	5 ml/min	10 ml/min	15 ml/min	5
Bacterial solution standing time ( $T_b$ )	1 h	3 h	5 h	8 h	12 h	5
Cement concentration ( $M_c$ )	0.25 M	0.5 M	0.75 M	1 M	1.5 M	5
Cement flow ( $Q_c$ )	1 ml/min	3 ml/min	5 ml/min	10 ml/min	15 ml/min	5
Cementation standing time ( $T_c$ )	1 h	3 h	5 h	8 h	12 h	5

Note. The concentration of bacterial liquid is characterized by its OD<sub>600</sub> value.

TABLE 2: Orthogonal design test condition.

ID	Test factor					
	Bacterial concentration ( $M_b$ )	Bacterial fluid flow ( $Q_b$ ) (ml/min)	Bacterial solution standing time ( $T_b$ ) (h)	Cement concentration ( $M_c$ ) (mol/L)	Cement flow ( $Q_c$ ) (ml/min)	Cementation standing time ( $T_c$ ) (h)
1#	0.25	1	1	0.25	1	1
2#	0.25	3	3	0.50	3	3
3#	0.25	5	5	0.75	5	5
4#	0.25	10	8	1.00	10	8
5#	0.25	15	12	1.50	15	12
6#	0.50	1	3	0.75	10	12
7#	0.50	3	5	1.00	15	1
8#	0.50	5	8	1.50	1	3
9#	0.50	10	12	0.25	3	5
10#	0.50	15	1	0.50	5	8
11#	1.0	1	5	1.50	3	8
12#	1.0	3	8	0.25	5	12
13#	1.0	5	12	0.50	10	1
14#	1.0	10	1	0.75	15	3
15#	1.0	15	3	1.00	1	5
16#	1.5	1	8	0.50	15	5
17#	1.5	3	12	0.75	1	8
18#	1.5	5	1	1.00	3	12
19#	1.5	10	3	1.50	5	1
20#	1.5	15	5	0.25	10	3
21#	2.0	1	12	1.00	5	3
22#	2.0	3	1	1.50	10	5
23#	2.0	5	3	0.25	15	8
24#	2.0	10	5	0.50	1	12
25#	2.0	15	8	0.75	3	1

TABLE 3: Physical properties of the sand used in this study [13].

Grain shape	Apparent density (g/cm <sup>3</sup> )	Water content (%)	Porosity (%)	Chemical composition	Grain size distribution (mm)
Round	2.65	0	40.5	>98% SiO <sub>2</sub>	0.075~0.60

surface. The main crack was dominated by the tensile failure surface (11#, 17#, 23#, and 24#).

**3.1.2. Stress-Strain Characteristics of Microbial Cemented Sand Body Structure.** Figure 5 shows the stress-strain curves of cemented sand columns under different control variables. It was observed from Figure 5 that (1) the overall deformation of the sand column under different control variables was small with the strain being within 2.5% at the peak strength; (2) the difference between the structures was large, with the peak strength of up to 7.33 MPa (14#, that is, OD<sub>600</sub>=1.0, Ca<sup>2+</sup> concentration was 0.75 mol/l working

condition), and the minimum strength being only at 0.21 MPa; and (3) stress-strain curve of microbial cemented sand body structure was different from the compression curve of brittle material, when the compressive strength reached the peak. Conversely, the curve does not fall quickly but presented a certain softening response. This characteristic phenomenon is consistent with the results observed in the literature [15]. From the overall trend of stress-strain in the figure, it is roughly divided into four stages, and the characteristics of each stage are as follows:

- (1) Pore compaction stage: during the initial stage of uniaxial compression of microbial cemented sand

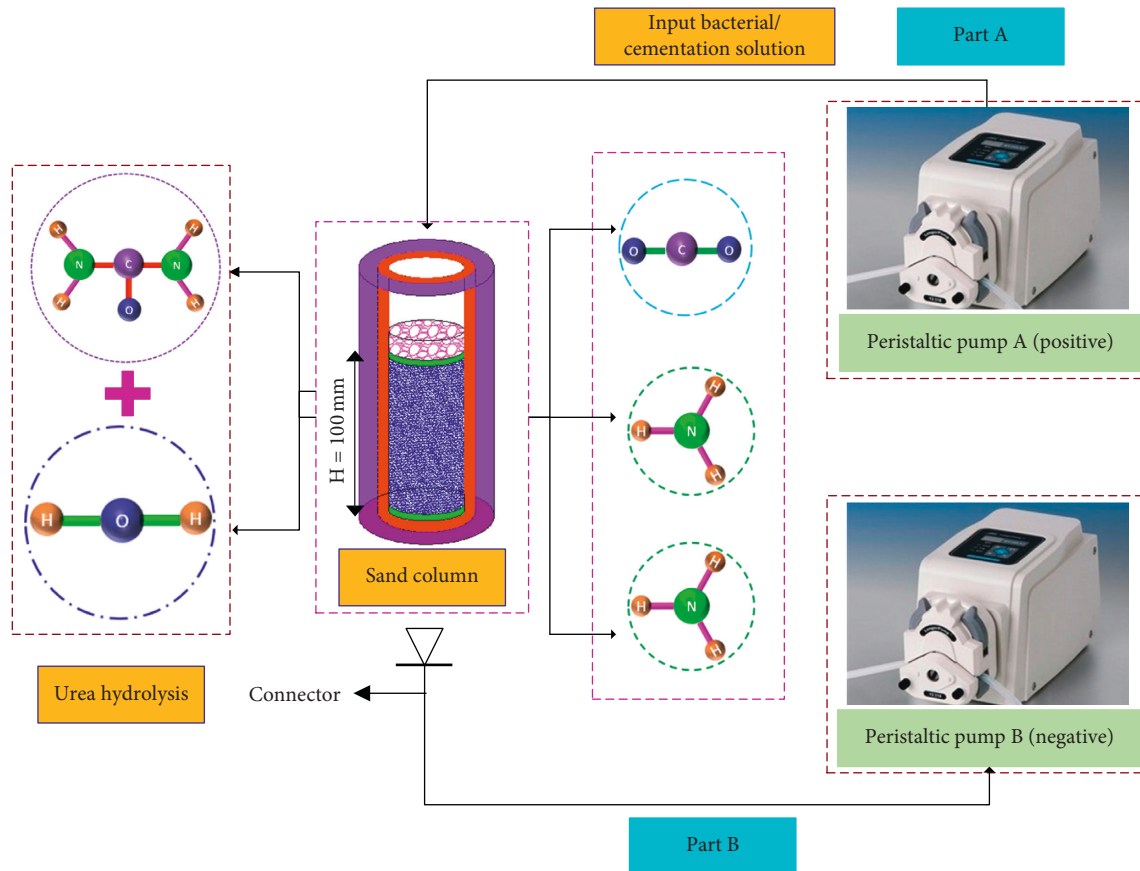


FIGURE 1: Experimental device.

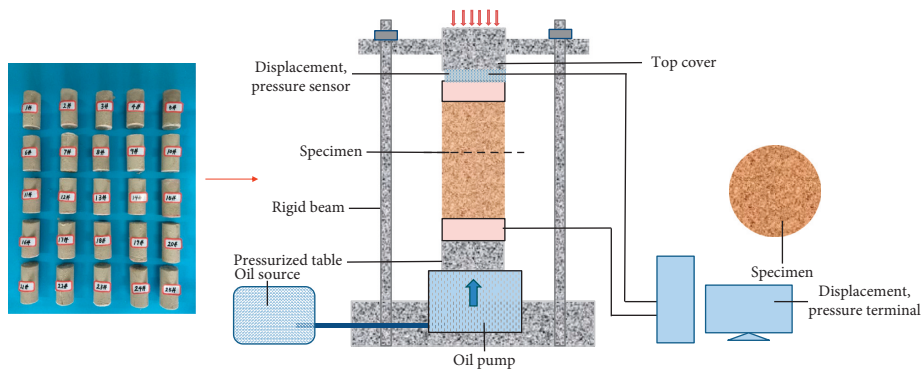


FIGURE 2: Uniaxial compression test.

body, the stress-strain curve appears as a concave section due to the continuous closure of the internal micropores, and the tangent modulus of each point on the curve gradually increases.

- (2) Elastic phase: the stress-strain curve at this stage changes linearly, i.e., the stress and strain are linear, the tangent modulus of each point remains basically unchanged, and the deformation of the microbial cemented sand body can be restored to elastic deformation.

- (3) Elastoplastic stage: after the microbial cemented sand body passes through the elastic stage, the stress-strain gradually enters the nonlinear stage, and the structural bearing capacity reaches the maximum at the peak time.
- (4) Postrupture stage: after the microbial cemented sand body reaches its peak value, the bearing capacity decreases greatly with the increase of deformation, and the tangent modulus of each point was negative with a significant softening phenomenon.

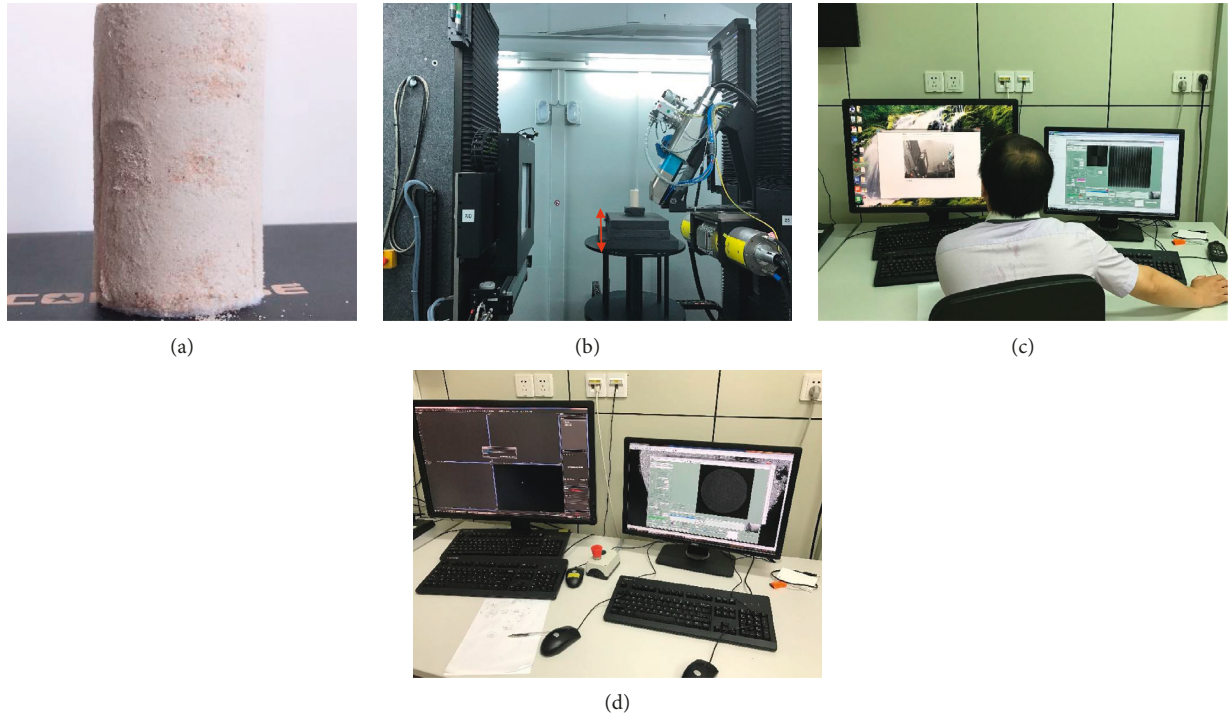


FIGURE 3: The micro-XCT experimental process [13]: (a) test sample selection; (b) placing and adjusting the sample position; (c) setting the parameters and scanning the sample; (d) feature extraction.



FIGURE 4: Picture of the uniaxial compression failure of the cemented sand column under different control variables.

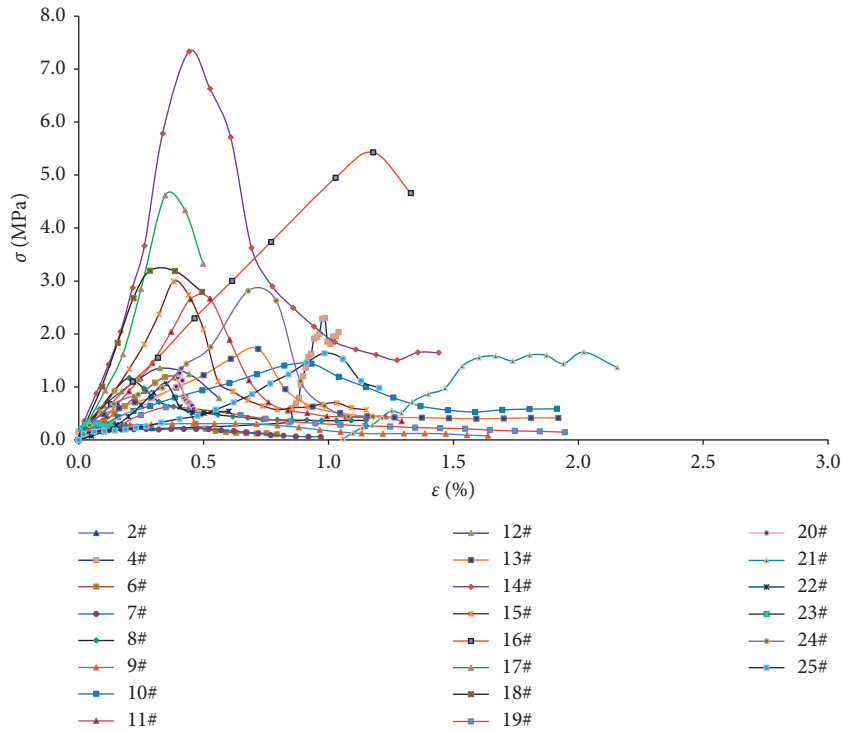


FIGURE 5: Stress-strain relationship curve of the cemented sand column.

For the strength difference between microbial cemented sand structures, this section introduces the calcium carbonate pore filling ratio to analyze the strength differences between structures. It should be noted here that the pore filling ratio of calcium carbonate reflects the filling of the crystal content inside the structure. The  $\text{CaCO}_3$  pore filling ratio  $P$  was calculated using the following formula:

$$P = \frac{V_{\text{CaCO}_3}}{V}, \tag{1}$$

where the cumulative volume of calcium carbonate ( $\text{cm}^3$ ) generated during the entire cementation process was the pore volume ( $\text{cm}^3$ ) before the cemented sand structure and the volume was 80 ml.

The relationship between the strength of the test sample and the pore filling ratio of calcium carbonate under different control variables is shown in Figure 6.

It can be seen from Figure 6 that (1) when the pore filling ratio,  $P\%$  of calcium carbonate is close and the compressive strength of cemented specimens is close (area A in the figure), and (2) the uniaxial compressive strength of cemented specimens increases as the filling ratio of calcium carbonate increases (dotted purple arrow). However, there are also cases where the filling ratio of calcium carbonate pore increases obviously and the strength decreases (dotted black arrow). For example, the pore filling ratio of calcium carbonate at 4.61 MPa and 3.20 MPa were significantly increased, but the strength continued to decrease.

In summary, the results show that there is an observable dependence of calcium carbonate pore filling ratio on the strength of microbial cemented sand body and that the  $P$  value causes the difference between structural strength. But,

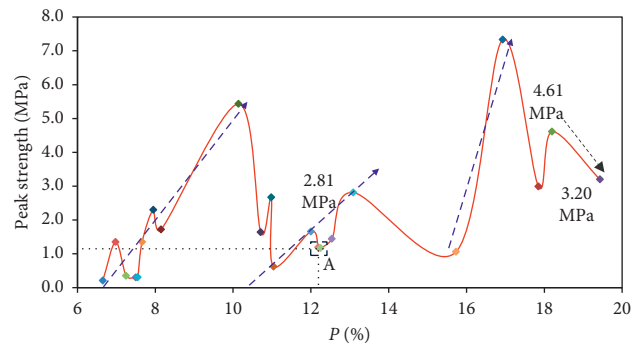


FIGURE 6: Relationship between test sample strength and calcium carbonate pore filling ratio under different control variables.

evidently the pore filling ratio of calcium carbonate is not the only influencing factor for the difference between the strengths. Additionally, the strength difference may also be affected by the mesostructure through analysis. The mechanism of correlation between mesostructural and mechanical properties has been analyzed in Section 3.2.

### 3.2. Study on the Correlation Mechanism between Mesostructure and Mechanical Properties of Cemented Sand Bodies.

Through the above analysis of the mechanical properties of the cemented sand body structure, it has been found that the mechanical properties of the structure are not only affected by the pore filling ratio of calcium carbonate but also are related to the mesostructure. According to the mechanical behavior of microbial cemented sand body structure under different control variables, 6 groups of XCT scanning tests

were carried out in this section. The corresponding strengths in the six groups of samples were 0.62 MPa, 1.66 MPa, 2.81 MPa, 3.20 MPa, 4.61 MPa, and 7.33 MPa. In order to improve the scanning accuracy, the sand column with a size of  $50 \times 50$  mm was selected for the XCT test. Thereafter, the XCT scanning technique was used to detect the distribution, crystal content, and dimensional change of the selected internal crystals of different strengths. In addition, the bonded sand body was analyzed, and also the mechanism of the correlation between mesostructural and mechanical properties was studied.

**3.2.1. Effect of Spatial Distribution and Content of Calcium Carbonate Crystal on Structural Strength.** In this paper, based on the analysis module within VG Studio Max 3.0 software, the sand and cement products in the sand column can be distinguished by defining the different parameters, and the crystal feature information (Figure 7(a)) was extracted by using the gray threshold algorithm.

In view of the large number of XCT scan layers, this section divided the scan samples into 200 layers and obtained the crystal content  $C\%$  of each scanning section. In the figure,  $S_C$  represents the sum of the areas of all crystals in a single-layer section, and  $S$  represents the total area of a single-layer section. Based on the analysis module in VG Studio Max 3.0 software, the proportion of crystals in the structure space was also counted, which was recorded as  $C_t\%$  (Figure 7(b)). In Figure 7(b),  $V_j$  represents a single crystal volume,  $N_j$  represents the number of crystals in equal volumes  $V_j$ , and  $V_c$  represents the total crystal volume. Based on the obtained  $C\%$  data of the crystal content of each scanning section, the curve of the single-layer crystal content in the height direction for six selective samples is shown in Figure 8.

In order to quantify the influence of the spatial distribution of the structure on the strength, this paper defined the index parameter  $C_f$  that characterizes the degree of material nonuniformity, for instance, for the uniform distributed crystals,  $C_f = 0$ , and for heterogeneous distributed crystals,  $C_f = 1$ .

The calculation formula is as follows:

$$C_f = \frac{\Delta C}{\Delta C_d} = \frac{C_{\max} - C_{\min}}{\Delta C_d} \quad (2)$$

In the formula,  $C_{\max}$  represents the maximum crystal content in the height direction of the single-layer crystal content and  $C_{\min}$  represents the minimum crystal content in the height direction of the single-layer crystal content.

According to the data in Figure 8, the maximum difference of crystal content corresponding to 3.20 MPa is 5.87, so the value is 5.87. Combined with equation (2), the results of the parameters calculated at different strengths are shown in Table 4.

From Table 4, the following points are observed: (1) The calcium carbonate crystals do not reach a true uniform distribution in the whole space ( $C_f > 0$ ). (2) For the spatial distribution of different crystals, there is a great difference in strength. The more uniform spatial distribution enhances

the structural strength of cemented sand body. For example, with a similar crystal content  $C_t\%$  (around 1.73%), the sample with  $C_f$  of 0.34 presents a higher strength (2.81 MPa) than the sample with  $C_f$  of 0.23 (0.62 MPa). (3) Increasing the crystal content helps to improve the structural strength for equal unevenness indicators  $C_f$ . For example, the strength noticeably improved for the two types of cemented sand body structures of  $C_f = 0.23$ , when the crystal content  $C_t\%$  increases from 1.28% to 1.73%. Similarly, there was a relatively small difference between the parameters  $C_f$  of the unevenness index for the cemented sand structure of  $C_f = 0.44$  and  $C_f = 0.47$ . However, due to the difference between the crystal contents, a significant difference in strength was seen in the final two  $C_f$  values.

In summary, the spatial distribution and crystal content of the crystal causes a change in strength. A more uniform spatial distribution of the crystal is conducive to improving structural strength. This is because, if the spatial distribution of the crystal is more uniform, it is more advantageous to improve the spatial network, thereby facilitating the structural load carrying capacity. Increasing crystal content  $C_t\%$  improves the structural strength under the premise that the spatial distribution of the crystal is similar, i.e., under the condition that  $C_f$  is equal. This is because the increase in crystal content helps to improve the cementation and packing inside the structure [16], which makes the structural integrity stronger, thus contributing to the structural strength. Consequently, the result of increasing the crystal content and increasing the strength is a good example of the influence of the porosity filling ratio  $P\%$  on the structural strength in Section 3.1.2.

Some differences have been observed for the two strength conditions of 3.20 MPa and 4.61 MPa mentioned in Section 3.1.2, combined with the data in Table 4 and the above analysis results, mainly due to the differences between crystal content and crystal space. But it does not rule out the influence of other factors, such as crystal size. Hence the analysis to be carried out in Section 3.2.3 has taken into consideration the effect of crystal size.

**3.2.2. Effect of Spatial Distribution of Calcium Carbonate Crystal on Structural Failure Mode.** Figure 9 shows the results of the comparison between the structural failure curves of the crystal spatial distribution at different strengths and the corresponding portions of the corresponding structures in Figure 4. It can be observed from Figure 9 that (1) the structure expands to both ends under load for a structure with a relatively uniform crystal space distribution, showing a failure mode dominated by tensile failure with a vertical straight line approximated as the failure curve (Figure 9(c)-CC1); (2) the failure mode dominated by shear failure is exhibited and a distinct shear rupture zone is formed for the structure in which the spatial distribution of the crystal is completely uneven with the curved line failure curve (Figure 9(a)-AA1, Figure 9(b)-BB1, Figure 9(d)-D1D2, and Figure 9(f)-F1F2); (3) a failure mode dominated by tensile-shear composite failure is exhibited forming distinct tensile and shear fracture zones for the spatial

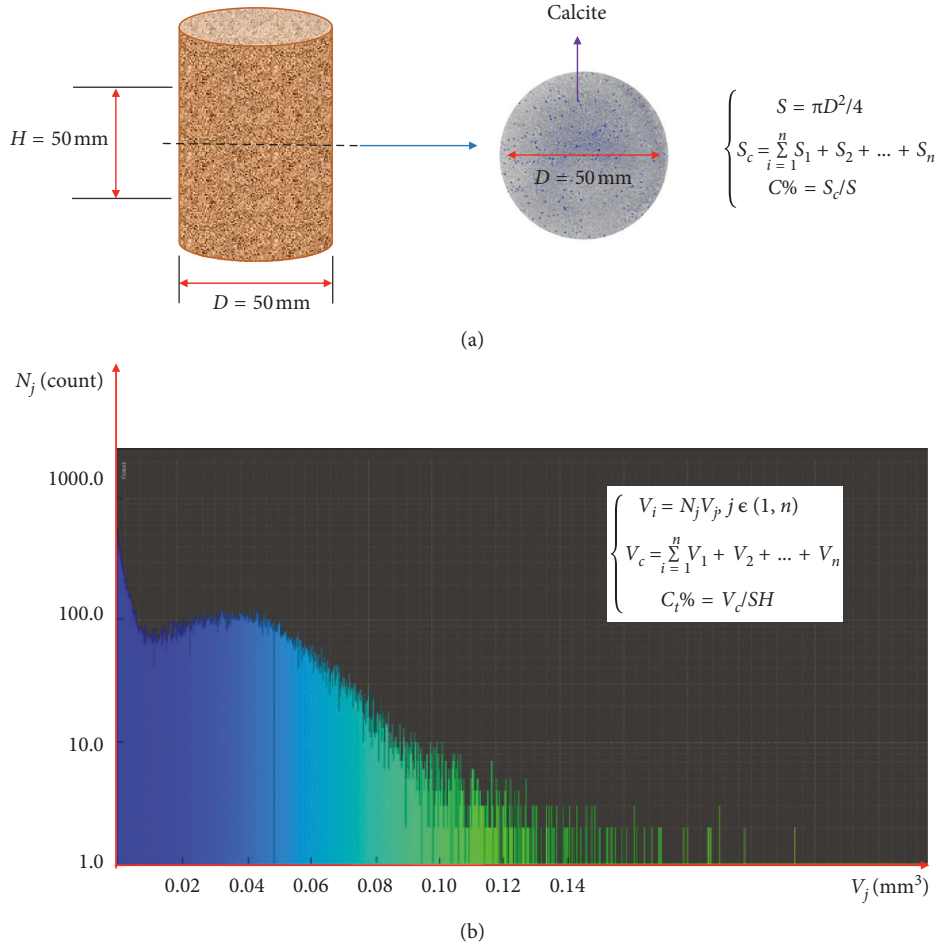


FIGURE 7: Extraction of characteristic information and crystal content statistics of calcium carbonate crystal. (a) Extraction of calcium carbonate crystal characteristic information. (b) Relationship between the number of calcium carbonate crystals and the corresponding volume (0.62 MPa).

distribution of crystals, including both uniform and non-uniform segments. The damage curve has both straight lines and curved lines (Figure 9(e)-E1E2). In addition, it has been found that the fracture curve turning position is usually the turning point of the maximum crystal content (point C1 in Figure 9(c)), and the expanding path of the breaking curve is synchronized with the crystal content from high to low. Therefore, there is high consistency between the spatial distribution curve of the crystal and the failure curve of the structure.

For a structure in which the spatial distribution of the crystal is relatively uniform, tensile stress will be generated in the lateral direction under the action of the axial compressive stress since the interlayer crystal content is substantially the same. As the axial stress increases, tensile failure occurs between the cemented sand particles, accompanied by continuous communication of the rupture zone, and eventually tensile failure occurs. For the structure in which the crystal content is completely unevenly distributed, the overall compactness of the interlayer structure is largely different due to the uneven distribution of interlayer crystal content, resulting in different positions of

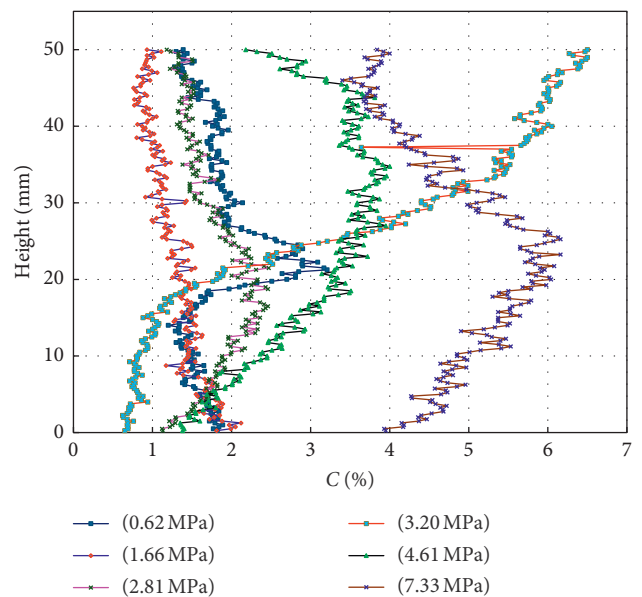


FIGURE 8: Distribution of single-layer crystal content along the height direction at different strengths.

TABLE 4: Index parameter results under different strengths.

Strength(MPa)	0.62	1.66	2.81	3.20	4.61	7.33
Uneven characteristic index $C_f$	0.34	0.23	0.23	1.0	0.44	0.47
Crystal content in the structural space $C_r\%$	1.74	1.28	1.73	1.06	2.85	4.43

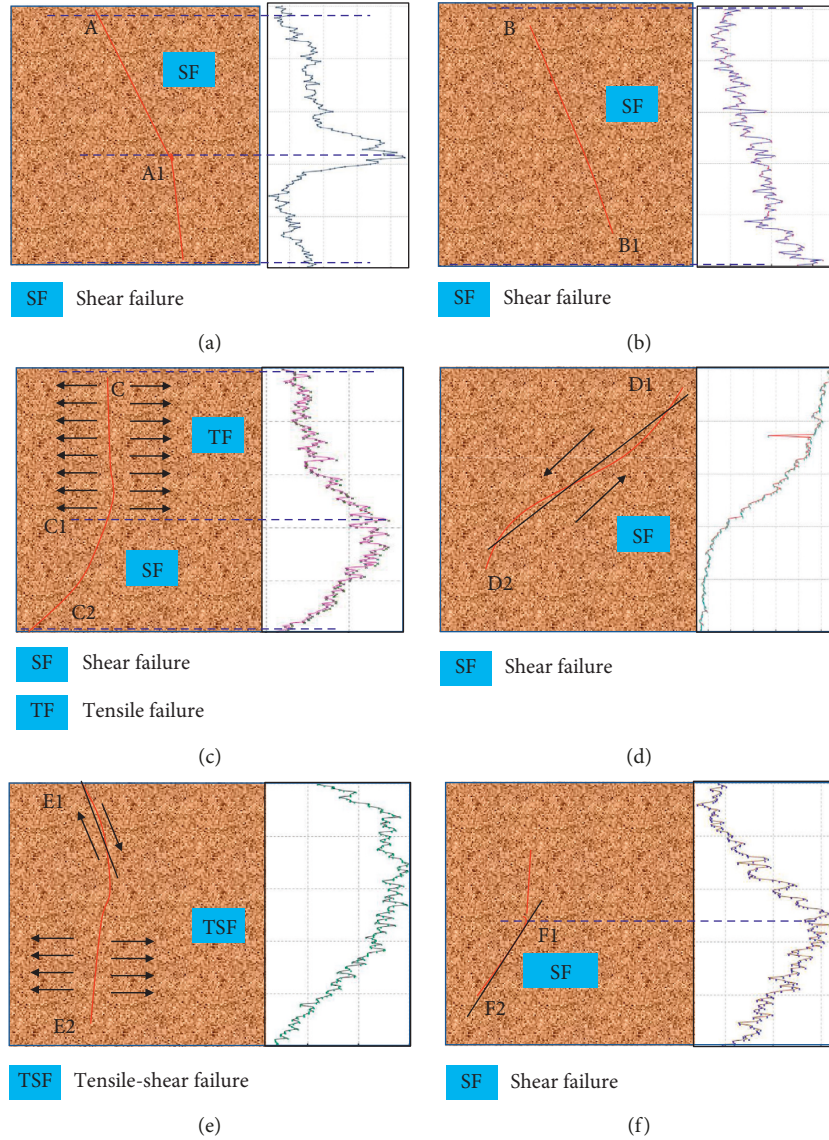


FIGURE 9: Comparison of structural failure modes and crystal spatial distribution at different strengths: (a) 0.62 MPa; (b) 1.66 MPa; (c) 2.81 MPa; (d) 3.20 MPa; (e) 4.61 MPa; (f) 7.33 MPa. TF: tensile failure; SF: shear failure; TSF: tensile-shear failure.

interlayer cementation. The microcrack propagation path usually develops along the path with the smallest structural impedance, such that it is most likely to break in the weaker part of the cementation, and finally the shear failure occurs. For a structure in which the spatial distribution of the crystal includes both a uniform segment and a nonuniform segment, it has tensile and shear failure characteristics, such that the tensile-shear composite failure eventually occurs.

It is found that the structural tensile failure, shear failure, and tensile-shear composite failure have observable

characteristics. The failure mode characterization was carried out by constructing the characteristic equation in order to better characterize the structural damage characteristics of different crystal spatial distribution. According to the spatial distribution characteristics of the crystal, it was divided into three cases:

- (1) For a structure with relatively uniform spatial distribution of the crystal, the damage curve was approximated characterized by a straight line (Figure 10(a)), with the equation as follows:

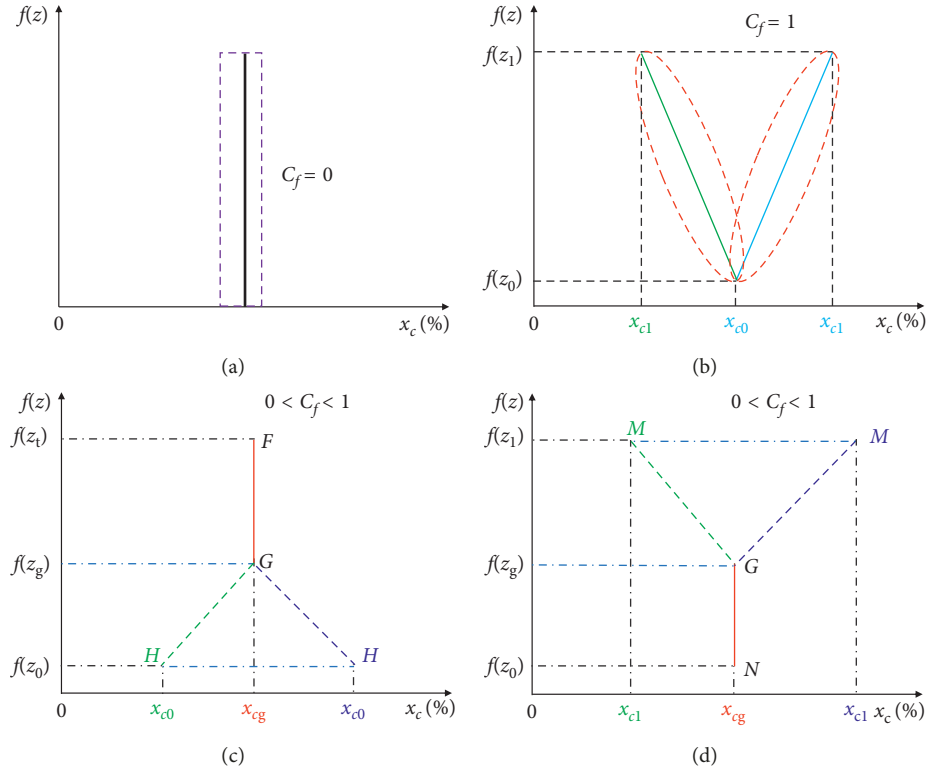


FIGURE 10: Corresponding simplified model for different crystal spatial distributions: (a) tensile failure; (b) shear failure; (c) first tension and then shear; (d) first shear and then tension.

$$\begin{cases} C_f = 0, \\ f(z) = x_c, \\ 0 < x_c. \end{cases} \quad (3)$$

- (2) For the structure of the heterogeneity characteristic with a completely unevenly distributed crystal content space, the damage curve can be simplified to an oblique line (Figure 10(b)), with the oblique line characteristic equation. Its characteristic equation is as follows:

$$\begin{cases} C_f = 1, \\ f(z) = kx_c = \frac{f(z_1) - f(z_0)}{|x_{c1} - x_{c0}|} x_c, \\ x_{c1} < x_{c0} \leq x_c, \\ x_{c0} < x_{c1} \leq x_c, \\ f(z_0) < f(z_1). \end{cases} \quad (4)$$

- (3) For a structure with both a uniform segment and nonuniform segment spatial distribution of crystal

content, the failure curve is presented as a straight line (Figure 10(c)-FG and Figure 10(d)-GN) for a relatively uniform crystal content and an oblique line (Figure 10(c)-GH and Figure 10(d)-MG) for the uneven crystal content. Since the failure mode is the tensile-shear composite failure, the failure mode has certain differences (first tension and then shear or vice versa), thus its characteristic equation is divided into two cases:

$$\begin{cases} 0 < C_f < 1, \\ f(z_t) = x_{cg}, \\ f(z_s) = kx_c = \frac{f(z_g) - f(z_0)}{|x_{cg} - x_{c0}|} x_c, \\ 0 \leq x_{c0} < x_{cg} \leq x_c, \\ 0 \leq x_{cg} < x_{c0} \leq x_c, \\ f(z_g) > f(z_0), \end{cases} \quad (5)$$

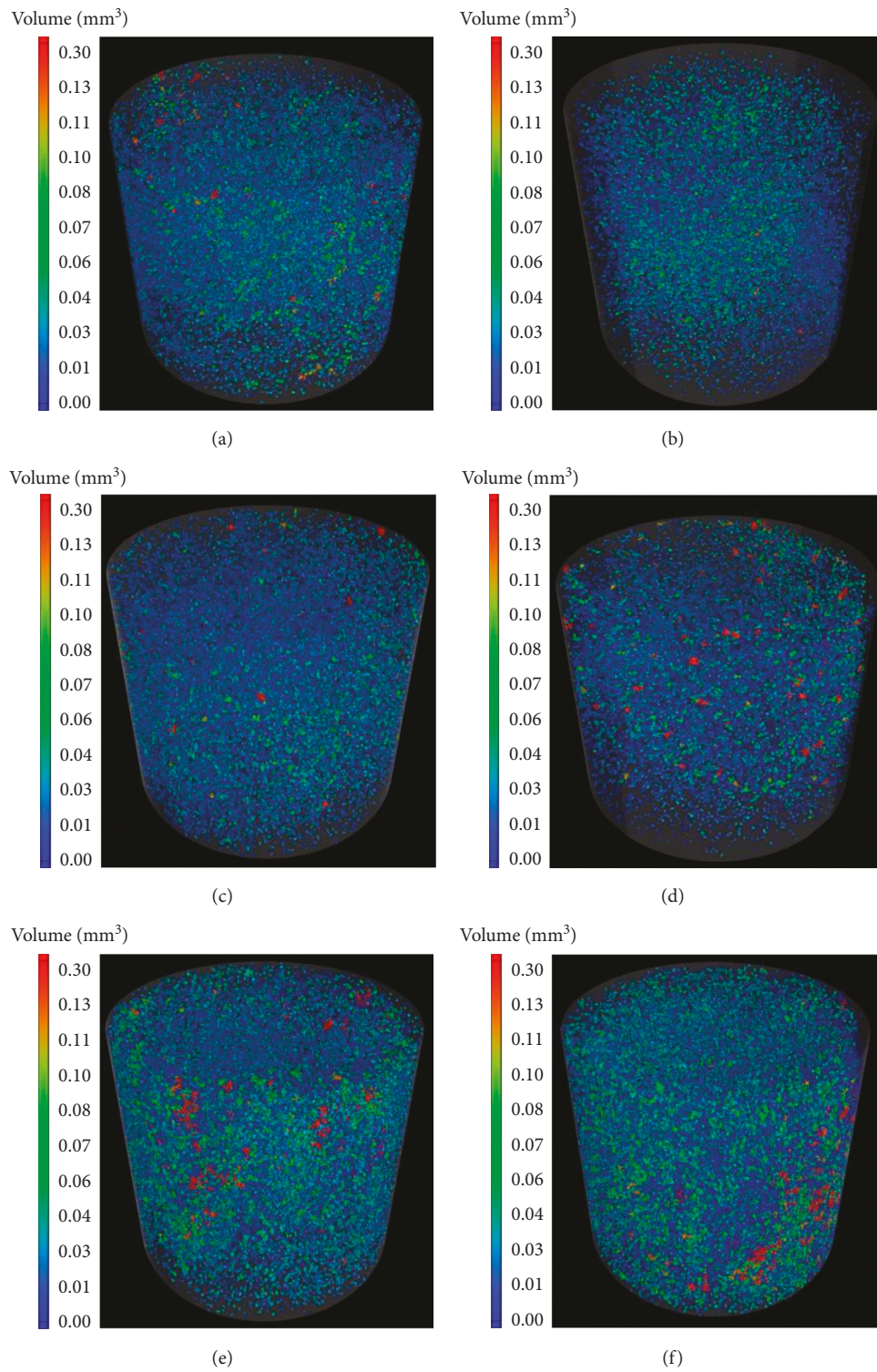


FIGURE 11: Crystal size changes at different strengths.

or

$$\left\{ \begin{array}{l} 0 < C_f < 1, \\ f(z_t) = x_{cg}, \\ f(z_s) = kx_c = \frac{f(z_1) - f(z_g)}{|x_{c1} - x_{cg}|} x_c, \\ x_{c1} < x_{cg} \leq x_c, \\ x_{cg} < x_{c1} \leq x_c, \\ f(z_1) > f(z_g), \end{array} \right. \quad (6)$$

where  $C_f$  represents the parameter of the nonuniform characteristic index,  $x_c\%$  represents the content of the crystal, and  $f(z)$  represents the height of the structure.

**3.2.3. Effect of Crystal Size Change of Calcium Carbonate on Structural Strength.** Based on the XCT scan data, the color scale in the software was used to identify the size of the calcium carbonate crystals, from blue to red, representing the crystal volume from small to large [17]. It can be seen that when the strength value is equal to 1.66 MPa (Figure 11(b)), the overall volumetric size of the internal calcium carbonate crystal is smaller, and most of the volume is less than  $0.04 \text{ mm}^3$ . When the strength value is equal to 2.81 MPa (Figure 11(c)), large volume crystal clusters (red) begin to appear. As the strength continues to increase, when the strength is equal to 4.61 MPa (Figure 11(e)), compared with 3.20 MPa (Figure 11(d)), the bulk crystal clusters and crystal content between  $0.06$  and  $0.14 \text{ mm}^3$  increased significantly. Notably, especially when the strength is equal to 7.33 MPa (Figure 11(f)), the bulk crystal clusters with volume ranging from  $0.06$  to  $0.14 \text{ mm}^3$  are the most abundant. Therefore, it can be deduced that the size of the internal crystal affects the structural strength, and increasing the crystal size can promote the structural strength improvement. For the observed differences in strength between 4.61 MPa and 3.20 MPa mentioned in Section 3.2.1, combined with the results of crystal size analysis, it is proved that the result of the spatial distribution of crystal, crystal content, and crystal size produced these differences in strength.

It should be noted here that for Figure 11(a), the crystal volume size is significantly larger than that of Figure 11(b), but the strength is low. This is mainly due to the uneven spatial distribution of crystals (Figure 8). For the uneven distribution of calcium carbonate crystals, it can lead to obvious difference in strength of the improved structure [18].

In summary, the strength of the microbial cemented sand body structure is closely related to the spatial distribution of the crystal, the crystal content, and the crystal size. Under the condition of ensuring relatively uniform spatial distribution, increasing the crystal content and increasing

the crystal size of the crystal help to increase the strength of the solidified sand column. This is because, under relatively uniform spatial distribution conditions, the crystal content is increased, which is beneficial to promote the complete construction of the “spatial network” structure in the initial sand particle medium. Under the action of microorganisms, the calcium carbonate crystals are continuously stacked and the crystal volume is changed with large internal pores of the sand column constantly being filled with crystals. Since the different pores are filled to make the solidified sample “structural” stronger, the structural compactness is continuously increased, such that the strength is improved [16]. In addition, the crystal-based spatial distribution curve and the structural failure curve have higher consistency characteristics, and the structural failure mode can be effectively predicted by analyzing the spatial distribution of the structural crystal.

## 4. Conclusion

Based on the orthogonal experimental design method, the mechanical properties of solidified sand samples under the combined action of six factors are discussed in this paper. Thereafter, the uniaxial compressive strength (UCS) test and X-ray computed tomography (XCT) were conducted to explore the macroscopic mechanical response and meso-structure characteristics of microbial cemented sand (MCS) materials in this paper. The following conclusions were drawn from the study:

- (1) The overall deformation of microbial cemented sand body is small, and the strain is less than 2.5% when the peak strength is reached. The stress-stress curve has obvious characteristics of pore compaction stage, elastic stage, elastic-plastic stage, and postfracture stage.
- (2) The strength has strong discreteness, and the content of crystal, spatial distribution of crystal, and crystal size significantly affect the strength of the structure.
- (3) Relatively uniform spatial distribution of the crystal facilitated to the initial construction of “spatial network” structure and further filling calcium carbonate crystal, characterized by the increased crystal content and crystal size, enhances the compressive strength.
- (4) Based on the high consistency of the spatial distribution curves of crystals and the structural failure characteristics, the failure modes of structures can be effectively predicted by analyzing the spatial distribution of structural crystals.

## Data Availability

The data used to support the findings of this study are included within the article.

## Conflicts of Interest

The authors declare that they have no conflicts of interest.

## Authors' Contributions

Yue Yan and Yang Tang conducted the experiments and wrote the manuscript, and Guobin Xu, Jijian Lian, and Dengfeng Fu analyzed data. All the authors reviewed the manuscript.

## Acknowledgments

The authors would like to acknowledge the support received from the National Key R&D Program of China (2016YFC0401904), Science Fund for Creative Research Groups of the National Natural Science Foundation of China (51621092), National Natural Science Foundation of China (51709198), and Tianjin Natural Science Foundation of China (Project number: 16JCQNJC07900).

## References

- [1] R. Siddique, V. Nanda, Kunal et al., "Influence of bacteria on compressive strength and permeation properties of concrete made with cement baghouse filter dust," *Construction and Building Materials*, vol. 106, pp. 461–469, 2016.
- [2] A. Sharma and R. Ramkrishnan, "Study on effect of Microbial Induced Calcite Precipitates on strength of fine grained soils," *Perspectives in Science*, vol. 8, pp. 198–202, 2016.
- [3] S.-G. Choi, K. Wang, and J. Chu, "Properties of biocemented, fiber reinforced sand," *Construction and Building Materials*, vol. 120, pp. 623–629, 2016.
- [4] N. H. Balam, D. Mostofinejad, and M. Eftekhari, "Use of carbonate precipitating bacteria to reduce water absorption of aggregates," *Construction & Building Materials*, vol. 141, pp. 565–577, 2017.
- [5] J. Chu, V. Ivanov, J. He, M. Naeimi, B. Li, and V. Stabnikov, "Development of microbial geotechnology in Singapore," in *Proceedings of Geo-Frontiers 2011*, pp. 4070–4078, Geotechnical Special Publication, Dallas, TX, USA, March 2011.
- [6] J. Chu, V. Ivanov, M. Naeimi et al., "Optimization of calcium-based bioclogging and biocementation of sand," *Acta Geotechnica*, vol. 9, no. 2, pp. 1–9, 2014.
- [7] H. Rong, *Preparation and Binding Mechanism of Microbe Cement*, Southeast University, Nanjing, China, 2014, in Chinese.
- [8] L. Cheng, M. A. Shahin, and D. Mujah, "Influence of key environmental conditions on microbially induced cementation for soil stabilization," *Journal of Geotechnical and Geoenvironmental Engineering*, vol. 143, no. 1, article 04016083, 2017.
- [9] N. K. Dhama, A. Mukherjee, and M. S. Reddy, "Micrographical, mineralogical and nano-mechanical characterisation of microbial carbonates from urease and carbonic anhydrase producing bacteria," *Ecological Engineering*, vol. 94, pp. 443–454, 2016.
- [10] L. Li, *Study on Tailings Cemented by Microbe and Process Technique*, Southeast University, Nanjing, China, 2013, in Chinese.
- [11] L. Chengxi and Z. Jun, "Nonlinear coupled dynamics analysis of A truss spar platform," *China Ocean Engineering*, vol. 30, no. 6, pp. 835–850, 2016.
- [12] J. P. Morgan, "Design and analysis: a researcher's handbook," *Technometrics*, vol. 47, no. 4, pp. 522–523, 2005.
- [13] Y. Tang, G. Xu, Y. Yan et al., "Thermal cracking analysis of microbial cemented sand under various strains based on the DEM," *Advances in Materials Science and Engineering*, vol. 2018, pp. 1–15, 2018.
- [14] G. Xu, Y. Tang, J. Lian, Y. Yan, and D. Fu, "Mineralization process of biocemented sand and impact of bacteria and calcium ions concentrations on crystal morphology," *Advances in Materials Science and Engineering*, vol. 2017, no. 19, pp. 1–13, 2017.
- [15] L. L. Min, S. N. Wei, and Y. Tanaka, "Stress-deformation and compressibility responses of bio-mediated residual soils," *Ecological Engineering*, vol. 60, no. 6, pp. 142–149, 2013.
- [16] M. Cui, J. Zheng, and H. Lai, "Experimental study on effect of particle size on strength of microbial solidified sand," *Rock and Soil Mechanics*, vol. S2, pp. 397–402, 2016, in Chinese.
- [17] Y. Tang, G. Xu, J. Lian, H. Su, and C. Qu, "Effect of temperature and humidity on the adhesion strength and damage mechanism of shotcrete-surrounded rock," *Construction and Building Materials*, vol. 124, pp. 1109–1119, 2016.
- [18] V. S. Whiffin, L. A. van Paassen, and M. P. Harkes, "Microbial carbonate precipitation as a soil improvement technique," *Geomicrobiology Journal*, vol. 24, no. 5, pp. 417–423, 2007.



**Hindawi**  
Submit your manuscripts at  
[www.hindawi.com](http://www.hindawi.com)

